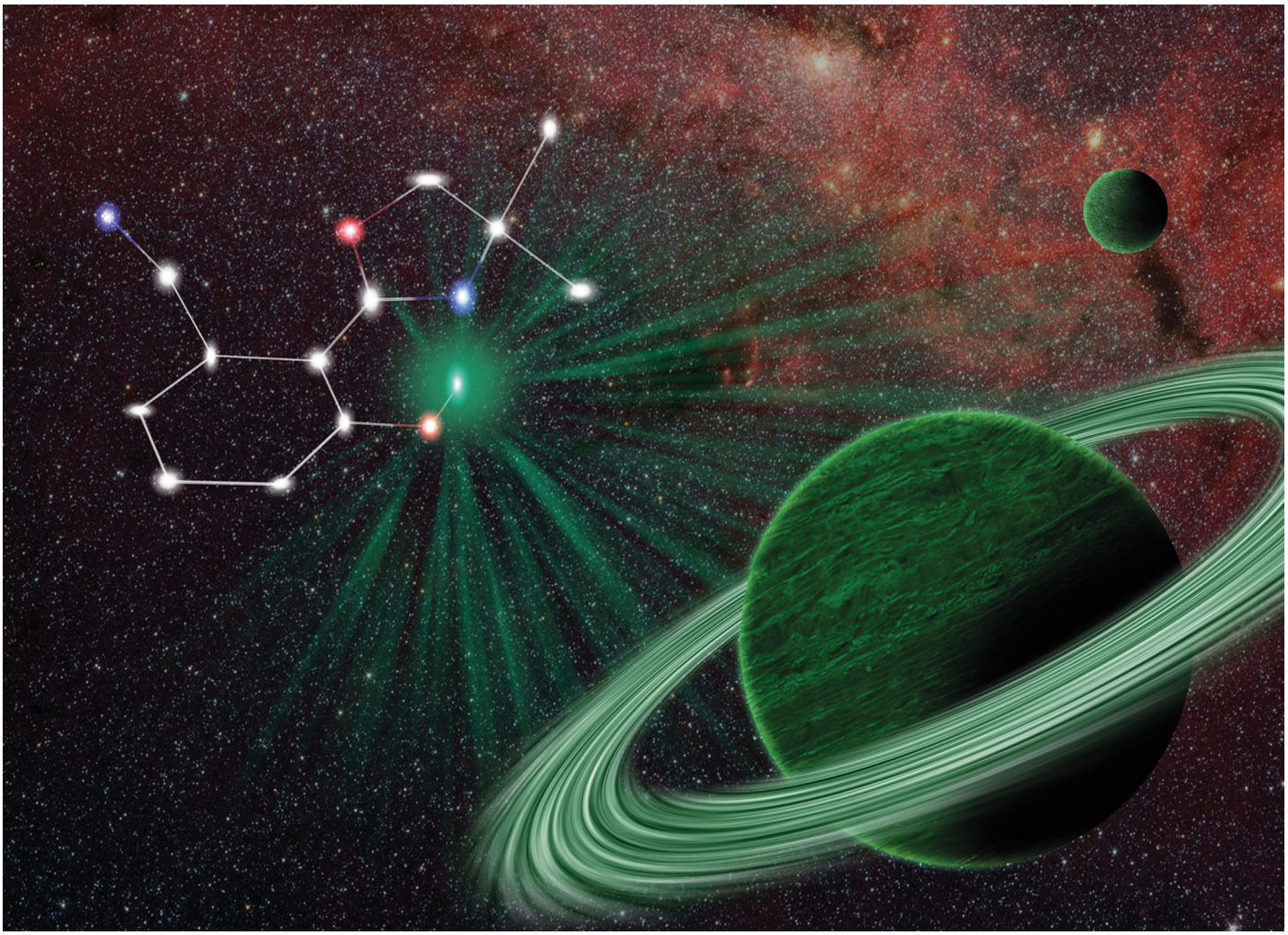

Showcasing research from Institute for Organic and Analytical Chemistry, University of Bremen, Germany

Nitrile-substituted 2-(oxazolinyl)-phenols: minimalistic excited-state intramolecular proton transfer (ESIPT)-based fluorophores

This work describes minimalistic, nitrile-substituted single-benzene, excited-state intramolecular proton transfer (ESIPT)-based fluorophores as powerful solid-state emitters. The outstanding photoluminescence properties were attributed to the well-shaped single crystal structure.

As featured in:

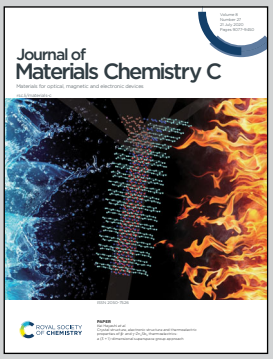

See Tim Stauch, Boris J. Nachtsheim *et al.*, *J. Mater. Chem. C*, 2020, **8**, 9213.

ROYAL SOCIETY OF CHEMISTRY

rsc.li/materials-c

Registered charity number: 207890

Journal of Materials Chemistry C

ROYAL SOCIETY OF CHEMISTRY

PAPER

View Article Online
View Journal | View Issue

Cite this: J. Mater. Chem. C, 2020, 8, 9213

Nitrile-substituted 2-(oxazolinyl)-phenols: minimalistic excited-state intramolecular proton transfer (ESIPT)-based fluorophores†

Dominik Göbel,[a] Daniel Duvinage,[b] Tim Stauch *[cde] and Boris J. Nachtsheim *[a]

Received 14th February 2020,
Accepted 30th April 2020

DOI: 10.1039/d0tc00776e

rsc.li/materials-c

Herein, we present minimalistic single-benzene, excited-state intramolecular proton transfer (ESIPT)-based fluorophores as powerful solid-state emitters. The very simple synthesis gave access to all four regioisomers of nitrile-substituted 2-(oxazolinyl)-phenols (M_W = 216.1). In respect of their emission properties they can be divided into aggregation-induced emission enhancement (AIEE) luminophores (**1-CN** and **2-CN**), dual state emission (DSE) emitters (**3-CN**) and aggregation-caused quenching (ACQ) fluorophores (**4-CN**). Remarkably, with compound **1-CN** we discovered a minimalistic ESIPT-based fluorophore with extremely high quantum yield in the solid state Φ_F = 87.3% at λ_{em} = 491 nm. Furthermore, quantum yields in solution were determined up to Φ_F = 63.0%, combined with Stokes shifts up till 11.310 cm^{-1}. Temperature dependent emission mapping, crystal structure analysis and time-dependent density functional theory (TDDFT) calculations gave deep insight into the origin of the emission properties.

Introduction

Highly emissive organic fluorophores have received great attention due to their intriguing and multifarious properties in the fields of biological imaging,[1] fluorescent sensors[2] and organic light-emitting diodes (OLEDs).[3] Commonly, three general strategies for the design of organic fluorescent frameworks are widely used – extended π-conjugated systems,[4] donor–acceptor (D–A) systems[5] and aggregation induced emission (AIE).[6,7] Extended π-conjugated systems based on a rigid and flat scaffold suffer from decreased solubility in conventional solvents. Furthermore, upon aggregation either in highly concentrated solution or in the solid state, their tendency of intermolecular π–π-stacking leads to radiationless quenching processes lowering the emission efficiency which results in low quantum yields. Contrarily, D–A systems are mostly constructed as small π-conjugated scaffolds, which are extensively used as fluorescent dyes and as luminophores in optoelectronic devices. The design and application of AIE-based luminophores have captured great attention in the recent two decades, since such structures such as siloles,[8] stilbenes[9] or arylethylenes,[10] show no or solely weak emission in solution but strong luminescence in the aggregated-state. With regard to biological application of organic fluorophores various properties are desirable. Small structures avoid impairing metabolite traffic within cells,[11] solid-state emission prevent fluorescent quenching[12] and a large Stokes' shifted emission minimizes the tendency of self-reabsorption.

The latter property is remarkably strong for excited-state intramolecular proton transfer (ESIPT)-based luminophores.[13] Such fluorophores are underlying to an enol–keto-phototautomerism cycle consisting of four levels, which causes the bathochromic-shifted emission and dual emission behavior (Scheme 1). Within this cycle, upon light absorption in the enol form, a phototautomerization on the subpicosecond timescale,[14] emission of the keto form and ground-state intramolecular proton transfer (GSIPT) takes place.

If the proton transfer in the excited state does not occur in a quantitative manner, dual emission[15] can be observed, which may result in white light generation.[16] Also, ESIPT-based luminophores have been identified as polymorph-dependent emitters,[17,18] color-tuning by substitution-effect luminophores[19] and amplified spontaneous emission molecules.[20,21]

Benzene is the simplest π-unit for the construction of luminescent systems. In general, emissive organic structures contain more than just one benzene ring either for conjugation or as substituent.

[a] Institute for Organic and Analytical Chemistry, University of Bremen, Leobener Straße NW2, D-28359 Bremen, Germany. E-mail: nachtsheim@uni-bremen.de
[b] Institute for Inorganic and Crystallographic Chemistry, University of Bremen, Leobener Straße NW2, D-28359 Bremen, Germany
[c] Institute for Physical and Theoretical Chemistry, University of Bremen, Leobener Straße NW2, D-28359 Bremen, Germany
[d] Bremen Center for Computational Materials Science, University of Bremen, Am Fallturm 1, D-28359 Bremen, Germany
[e] MAPEX Center for Materials and Processes, University of Bremen, Bibliothekstraße 1, D-28359 Bremen, Germany

† Electronic supplementary information (ESI) available: Detailed experimental procedures, characterization data, photophysical data, X-ray crystallographic data, and copies of ^{1}H-, ^{13}C-NMR spectra. CCDC 1908035, 1970920 and 1970921. For ESI and crystallographic data in CIF or other electronic format see DOI: 10.1039/d0tc00776e

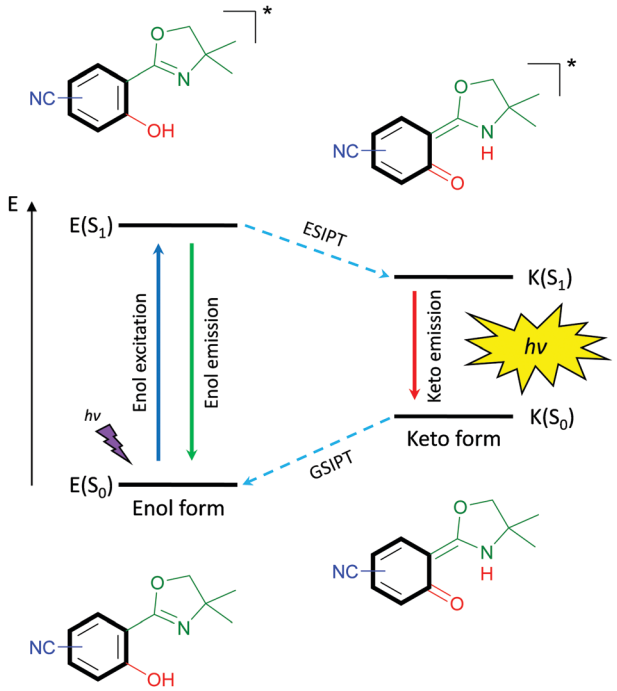

Scheme 1 Schematic representation of the ESIPT-process.

The design of minimalistic, single-benzene based, organic molecules exhibiting bright solid-state fluorescence is of fundamental interest and extremely challenging. Despite the supposedly straightforward synthesis of such simple structures, literature examples of low molecular weight, highly emissive molecules are extremely rare.

Efficacious known single-benzene luminophores can be divided into two categories – D–A based X-shaped structures and ESIPT-based molecules (Fig. 1). The popular tetrasubstituted X-shaped design of benzene with two electron-donating groups (EDGs) and two electron-withdrawing groups (EWGs) was first reported by Shimizu's group with the development of 1,4-bis(alkenyl)-2,5-dipiperidinobenzenes (Fig. 1a).[22] Through the judicious choice of EWGs on the alkenyl side arm, the solid-state emission could be tuned across the full-color spectrum. In the following, Katagiri's group published 2,5-bis(methylsulfonyl)-1,4-phenyldiamine, which displayed green pH-independent and blue solid-state emission properties (Fig. 1b).[23] In 2017, Zhang and coworkers developed dimethyl 2,5-bis-(methylamino)terephthalate, exhibiting a strong red emission (Fig. 1c).[24] Very recently, full color range tuning was also achieved by Yuan's group through fully substituted 2,5-bis(alkylamino)-3,6-difluoroterephthalonitriles (Fig. 1d).[25] X-shaped single-benzene fluorophores suffer from drawbacks like strong intra- and intermolecular hydrogen-bonding and the highly substituted character, which strongly restrict further derivatization and emission tuning. Potent low molecular weight ESIPT-based luminophores are truly rare, since potent structures are commonly constructed using π-extended proton acceptors such as benzazoles.[26] Chuo and co-workers reported hydroxylated analogues of the green fluorescent protein chromophore, which display rather weak emission in solution (up to $\Phi_F = 12\%$) but strong yellow emission in the solid state (Fig. 1e).[27] (2-Hydroxyphenyl)propenone derivatives

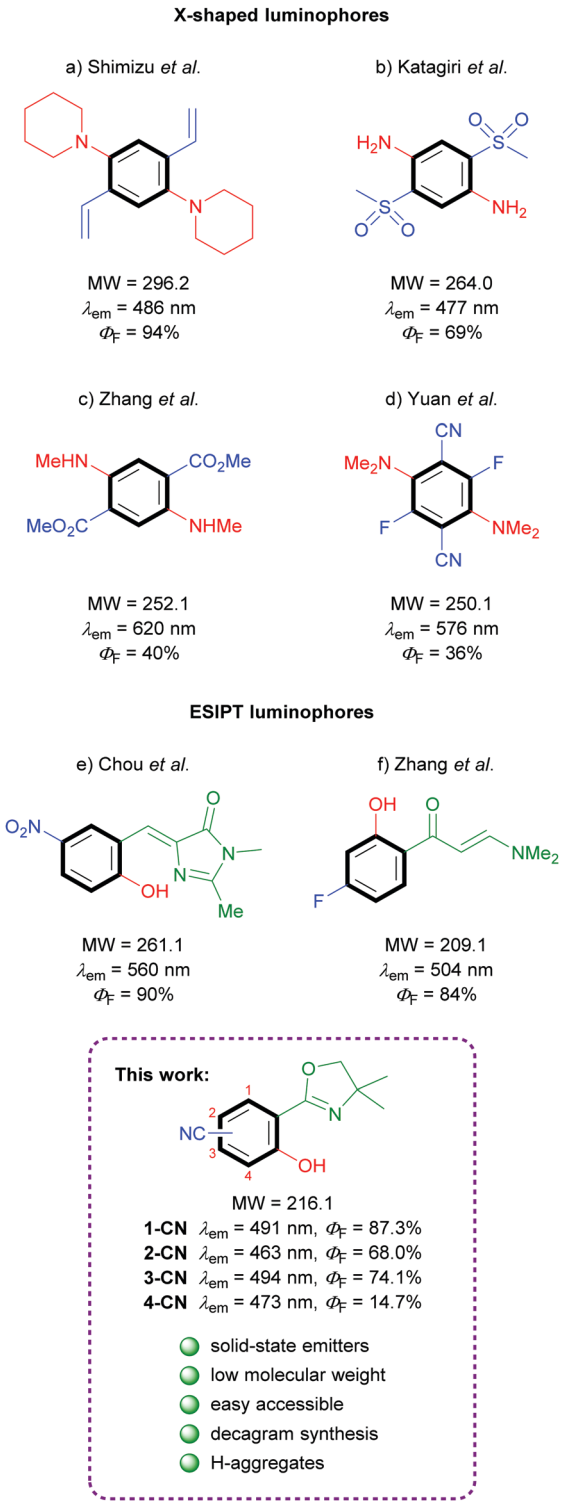

Fig. 1 Literature examples of single-benzene solid-state emitters.

exhibiting no emission in solution but efficient green crystal emission were published by Zhang's group (Fig. 1f).[21] While all these investigations were based on the search of efficient functional groups achieving high solid-state quantum yields for the given chromophore, the power of different regioisomers was never examined in detail.

In the course of our investigation toward minimalistic and highly emissive luminophores we observed phenol generation of magnesiated 2-aryloxazolines upon exposure to air or molecular oxygen as sustainable oxygen sources.[28,29] The so developed deprotonative hydroxylation protocol delivered full colored ESIPT-based fluorophores as already shown in initial examinations. Herein, we report nitrile-substituted *ortho*-hydroxy-2-phenyloxazolines as extremely efficient, low molecular weight, single-benzene fluorophores (Fig. 1; bottom). All four possible regioisomers were synthesized and analyzed comprehensively in terms of photophysical properties, crystal structures and theoretical calculations.

Results and discussion

Syntheses

Nitrile-substituted phenols were achieved starting from formylbenzonitriles, which were transformed to the corresponding 2-aryloxazolines (**1-Oxa**, **2-Oxa** and **3-Oxa**) in very good yields *via* a two steps sequence including condensation with 2-amino-2-methylpropan-1-ol and subsequent oxidation using NBS (Scheme 2, entry 1).[30] Phenol incorporation was accomplished by *ortho*-directed metalation using TMPMgCl·LiCl and ensuing smooth hydroxylation with molecular oxygen providing the desired phenols (**1-CN**, **2-CN** and **3-CN**) in excellent yields (Scheme 2, entries 2–4).[28] To our delight, hydroxylation of **2-Oxa** delivered besides the major isomer **2-CN** also the minor regioisomer **4-CN**, even though in low yields. Summarizing, this synthetic route demonstrates the simplicity of achieving these highly potent luminophores. To further demonstrate the robustness of our synthetic approach we performed the synthesis of **1-CN** in a scale-up reaction and achieved this structure on a decagram scale (see the ESI,† Chapter 2.4).

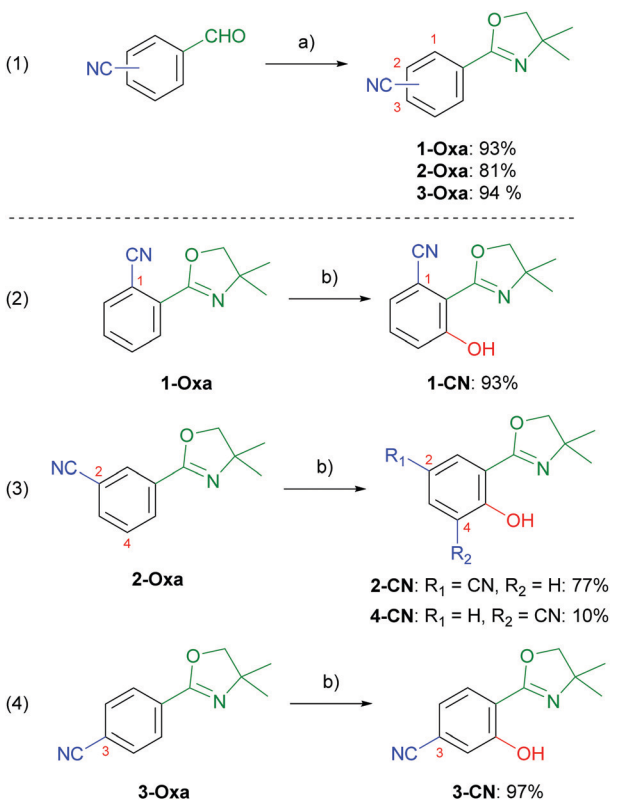

Scheme 2 (a) (1) 2-amino-2-methylpropan-1-ol, 4 Å MS, CH_2Cl_2, 25 °C, 20 h; (2) NBS, CH_2Cl_2, 25 °C, 4 h; (b) (1) TMPMgCl·LiCl, THF, 25 °C, 1 h; (2) O_2 (1 atm), 25 °C, 24 h. NBS = *N*-bromosuccinimide, TMP = 2,2,6,6-tetramethylpiperidinyl.

Absorption properties

With all regioisomers of nitrile-substituted phenols (**1-CN**, **2-CN**, **3-CN** and **4-CN**) in hand, we started to investigate their photophysical properties. UV-vis absorption spectra were measured in seven solvents exhibiting differing polarities, *i.e.*, methanol (MeOH), acetonitrile (ACN), ethyl acetate (EtOAc), 2-methyltetrahydrofuran (2-MeTHF), dichloromethane (DCM), toluene (PhMe) and cyclohexane (CH). Generally, the absorption properties of the respective luminophore are widely solvent independent (Table 1; see the ESI,† Fig. S22, S48, S72, S96 and Table S1, ESI†), while slight differences are detectable in the same solvent (Fig. 2a). In DCM solution, intense absorption bands deriving from the single-benzene core are visible below 280 nm, which are indicative of typical π–π^* transitions. Furthermore, broad and unstructured absorption bands are detected with maxima λ_{abs} between 303 and 326 nm and extinction coefficients ranging from 5300 to 8850 mol L^{-1} cm^{-1} (Fig. 2a and Table 1). The excitation spectrum of **3-CN** in CH_2Cl_2 indicates a maximum population of the excited-state upon irradiation in the absorption band with a maximum at 326 nm, while bands below 280 nm show diminished transitions for emission at 468 nm (Fig. 2b).

Fluorescence properties in solution

Complementary to absorption measurements, fluorescence properties **1-CN**, **2-CN**, **3-CN** and **4-CN** were studied in solvents with distinctive dipole moments – *i.e.*, MeOH, ACN, EtOAc, 2-MeTHF, DCM, PhMe, CH. The results are listed in Table 1. Excitation in the respective absorption maxima resulted in blue to cyanic emission maxima λ_{em} (445 nm to 487 nm) depending on the structure and the utilized solvent (Fig. 3). Notably, **1-CN** and **3-CN** emit in average 10 to 20 nm more red-shifted than **2-CN** and **4-CN**. Dual emission behavior, which could be caused by the enol–keto-phototautomerization, was never identified. Slight solvatochromism is observed as expected for ESIPT-based structures. Protic, polar solvents such as methanol result in blue-shifted emission due to phenol coordination, while with decreasing solvent polarity a red-shifted emission can be detected as displayed for **1-CN**, **2-CN**, **3-CN** and **4-CN** (Fig. 4). Due to their ESIPT-based character, all phenols exhibit large Stokes' shifted emission of up to 11.310 cm^{-1}, which resulted in baseline separated absorption and emission bands (Fig. 2b). Hence, highly efficient proton transfer in the excited state takes place for all phenols in all solvents, indicating that emission exclusively originate from the keto tautomer. Quantum yields (Φ_F) in solution show a significant solvent-dependency as well. Lowest quantum yields are usually observed for CH, while highest values are observed for DCM, ACN and EtOAc. For **1-CN** Φ_F ranges from 8.2% (CH) to 24.9% (DCM), while for **2-CN** Φ_F ranges from 15.1% (CH) to 25.2% (DCM). Significantly higher quantum yields in solution

Table 1 Photophysical data of **1-CN**, **2-CN**, **3-CN** and **4-CN** measured in aerated solution at 295 K

Compd	Solvent	λ_{abs} [nm] (ε [mol L^{-1} cm^{-1}])	λ_{em} [nm]	$\Delta\tilde{\nu}$ [cm^{-1}]	Φ_F[a] [%]	τ[b] [ns] (Rel%)	k_r[c] [10^8 s^{-1}]	k_{nr}[c] [10^8 s^{-1}]
1-CN	MeOH	321	467	9740	13.7	1.87 (71.6) 2.87 (28.4)	0.64	4.00
	ACN	320	471	10 020	15.2	2.08	0.73	4.07
	EtOAc	320	473	10 110	15.6	2.34	0.67	3.61
	2-MeTHF	321	476	10 140	14.0	2.07 2.11[d]	0.68	4.16
	THF	321	477	10 190	17.2	2.38 (92.5) 5.10 (7.5)	0.67	3.21
	DCM	322 (5790)	471	9820	24.9	3.09	0.81	2.43
	PhMe	322	477	10 090	18.1	2.31 (21.5) 7.09 (78.5)	0.30	1.35
	CH	322	481	10 270	8.2	1.13	0.73	8.16
2-CN	MeOH	303	445	10 530	20.5	2.71	0.76	2.94
	ACN	301	449	10 950	16.0	2.35	0.68	3.57
	EtOAc	303	454	10 980	24.7	2.86	0.86	2.64
	2-MeTHF	304	455	10 920	22.1	2.88	0.77	2.70
	DCM	303 (5300)	452	10 880	25.2	3.30	0.76	2.27
	PhMe	306	462	11 040	22.3	6.74	0.33	1.15
	CH	306	468	11 310	15.1	2.04	0.74	4.17
3-CN	MeOH	323	465	9450	51.0	2.53 (5.5) 7.60 (94.5)	0.70	0.67
	ACN	324	465	9360	49.4	7.29	0.68	0.69
	EtOAc	326	468	9310	47.4	6.75	0.70	0.78
	2-MeTHF	327	469	9260	47.0	6.53 7.67[d]	0.72	0.81
	DCM	326 (5790)	468	9310	55.6	8.10	0.69	0.55
	PhMe	328	479	9610	55.0	8.95	0.61	0.50
	CH	327	487	10 050	39.7	6.02	0.66	1.00
4-CN	MeOH	320	454	9220	49.8	5.27	0.95	0.95
	ACN	319	456	9420	40.5	5.30	0.76	1.12
	EtOAc	320	459	9460	63.0	5.22	1.21	0.71
	2-MeTHF	321	462	9510	48.7	5.14	0.95	1.00
	DCM	321 (8850)	457	9270	52.9	5.52	0.96	0.85
	PhMe	322	469	9730	52.4	7.92	0.66	0.60
	CH	322	479	10 180	44.8	5.10	0.88	1.08

[a] Absolute quantum yields were determined by using an integration sphere. [b] Relative ratio of the species of a double exponential function are given in parentheses. [c] k_r (10^8 s^{-1}) and k_{nr} (10^8 s^{-1}) were calculated using the equations $k_r = \Phi_F/\tau$ and $k_{nr} = (1 - \Phi_F)/\tau$. [d] Half lifetimes were measured after bubbling with argon for 30 minutes.

were measured for **3-CN** ranging from 39.7% (CH) to 55.6% (DCM) and for **4-CN** from 40.5% (ACN) to 63.0% (EtOAc). Fluorescence half lifetimes (τ) of the excited state were determined by time correlated single photon counting (TCSPC). Similar tendencies were observed for all phenols, with lowest half lifetime values in CH, ranging from 1.13 ns (**1-CN**) to 6.02 ns (**3-CN**), and highest values in DCM, ranging from 3.09 ns (**1-CN**) to 8.10 ns (**3-CN**). Fluorescence half lifetimes are significant higher in PhMe, ranging from 7.09 ns (**1-CN**, major species of biexponential decay) to 8.95 ns (**3-CN**). To investigate the role of aerated *vs.* deaerated media, 2-MeTHF solutions of **1-CN** and **3-CN** were bubbled with argon for 30 minutes and measured again. For **1-CN** no prolonged fluorescence half lifetimes were observed (see Fig. S13, ESI†), while the **3-CN** solution shows a significant half lifetime increase by a factor of 1.17 (6.53 ns to 7.67 ns) (see Fig. S63, ESI†). With values of Φ_F and τ in hand, the radiative (k_r) and nonradiative (k_{nr}) decay rate constants were determined according to the equations $k_r = \Phi_F/\tau$ and $k_{nr} = (1 - \Phi_F)/\tau$.

For phenols showing high emission in solution radiative decay rates k_r ranging from 0.68×10^8 s^{-1} (**3-CN** in ACN) to 1.21×10^8 s^{-1} (**4-CN** in EtOAc) and nonradiative decay rates k_{nr} ranging from 0.50×10^8 s^{-1} (**3-CN** in PhMe) to 1.12×10^8 s^{-1} (**4-CN** in ACN) were observed. These values indicate the suppression of nonradiative decay pathways and preferred radiative decays for **3-CN** and **4-CN** in solution.

Fluorescence at low temperatures

To shed light on the temperature dependent emission behavior, deaerated 2-MeTHF solutions of **1-CN**, **2-CN**, **3-CN** and **4-CN** were examined and temperature maps were created by measuring in 40 K intervals down to 80 K (Fig. 5 and Table 2). A steady increase in photoluminescence intensity was observed upon cooling of **1-CN** solution with maximum intensity detected at 80 K (Fig. 5a and b). This occurrence is unusual for ESIPT-based luminophores due to the typical suppression of the emission process at deep temperatures. Compared to 295 K the emission intensity is multiplied by the factor of 5.65 at 80 K. Additionally,

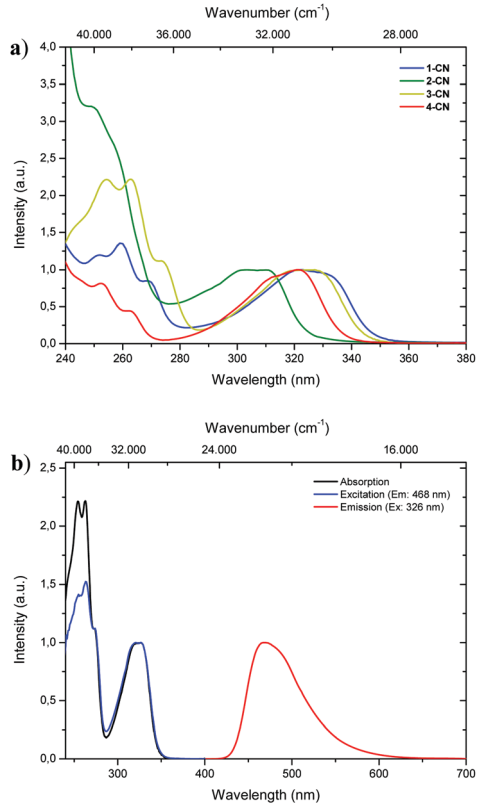

Fig. 2 (a) Normalized UV-vis absorption spectra of **1-CN** (blue line), **2-CN** (green line), **3-CN** (yellow line) and **4-CN** (red line) in CH_2Cl_2. (b) Normalized absorption (black line), excitation (blue line) and emission spectra (red line) of **3-CN** in CH_2Cl_2.

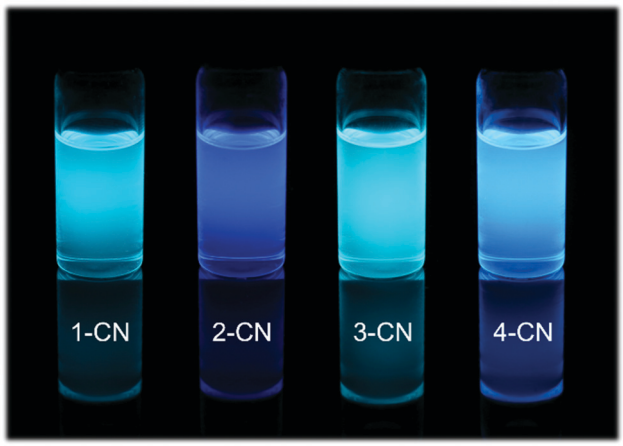

Fig. 3 Representative images of **1-CN**, **2-CN**, **3-CN** and **4-CN** in CH_2Cl_2 solution at $c = 10^{-4}$ mol L^{-1} under 366 nm irradiation.

a significant blue-shifted emission was detected while cooling below 200 K with a wavelength of 462 nm at 80 K emission maximum (Fig. 5c). Analyzing the temperature dependent emission of **3-CN** in 2-MeTHF indicates an increasing intensity up to 160 K (factor 1.66 compared to 295 K) followed by a decrease in intensity (Fig. 5d and e). This behavior of a lowered intensity below a certain temperature is in accordance with known ESIPT-based emitters.[17]

Again, linear blue-shifted emission was detected with a minimal emission wavelength of 456 nm at 80 K (Fig. 5f). Importantly, both temperature maps (Fig. 5a and d) display the disappearance of the broad emission band at 295 K and splitting into at least two definite bands. Owing to suppressions of intramolecular degrees of freedom line broadening is significantly reduced, resulting in the given pattern. Temperature maps of **2-CN** and **4-CN** show similar behavior as **3-CN** (see the ESI,† Chapters 3.2.2 and 3.4.2).

Next, fluorescence half lifetimes (τ) of the excited states at 80 K were determined for all phenols in deaerated 2-MeTHF by TCSPC. Remarkably, half lifetimes were prolonged in average and triple exponential decays were observed for **1-CN**, **2-CN** and **3-CN** (Fig. 6 and Table 2). Long living species with half lifetimes ranging from 23.0 ns (**2-CN**) to 44.0 ns (**1-CN**) were detected in lower population. Only, **4-CN** showed a contrary behavior with only one single emitting species, which exhibits a slightly increased half lifetime compared to measurements at 295 K. It is worth mentioning that long living triplet emission (phosphorescence) or thermally activated delayed fluorescence (TADF) was never observed during our investigations, neither at rt nor at 80 K.

Aggregation induced emission enhancement

Fluorophores which show no emissive or low emissive properties in solution can become highly emissive in the solid state. Several mechanisms for the emission enhancement like the restriction of intramolecular vibrational and rotational motions (RIM), intramolecular charge transfer (ICT)[31] or twisted intramolecular charge transfer (TICT) are well known and result in the phenomenon called aggregation-induced emission (AIE) and aggregation-induced emission enhancement (AIEE).[6,7] We chose **1-CN** for further investigations towards aggregation-induced emission and utilized tetrahydrofuran (THF) as a non-aggregating solvent and water as the aggregating solvent.[32] In the course of the investigation, the concentration was kept at 4×10^{-5} mol L^{-1}. Initially, as depicted in Fig. 7a, fluorescence is already present at low water fractions (f_w = 10%), as confirmed by emission properties of pure THF solution (λ_{em} = 477 nm, Φ_F = 17.2% (Table 1)).

With increasing water fractions of up to f_w = 90%, a moderate emission enhancement is detected with a slight drop of emission intensity (Fig. 7b) at f_w = 50% (λ_{em} = 466 nm) and f_w = 90% (λ_{em} = 460 nm) including a blue-shifted emission (Fig. 7c). This hypsochromic shift, starting from f_w = 10% to f_w = 90% can be explained by the increasing polarity of the surrounding medium, which is in accordance with emission wavelength tendencies for polar solvents like methanol, reasoned by phenol coordination. Interestingly, further water addition to f_w = 95% resulted in a red-shifted emission (λ_{em} = 478 nm) and an increase of intensity. Maximum emission boosting was obtained at f_w = 99% with another significant red-shift (λ_{em} = 488 nm) and almost doubling of fluorescence intensity, which resulted in a quantum yield of Φ_F = 41.3%. Within the last two

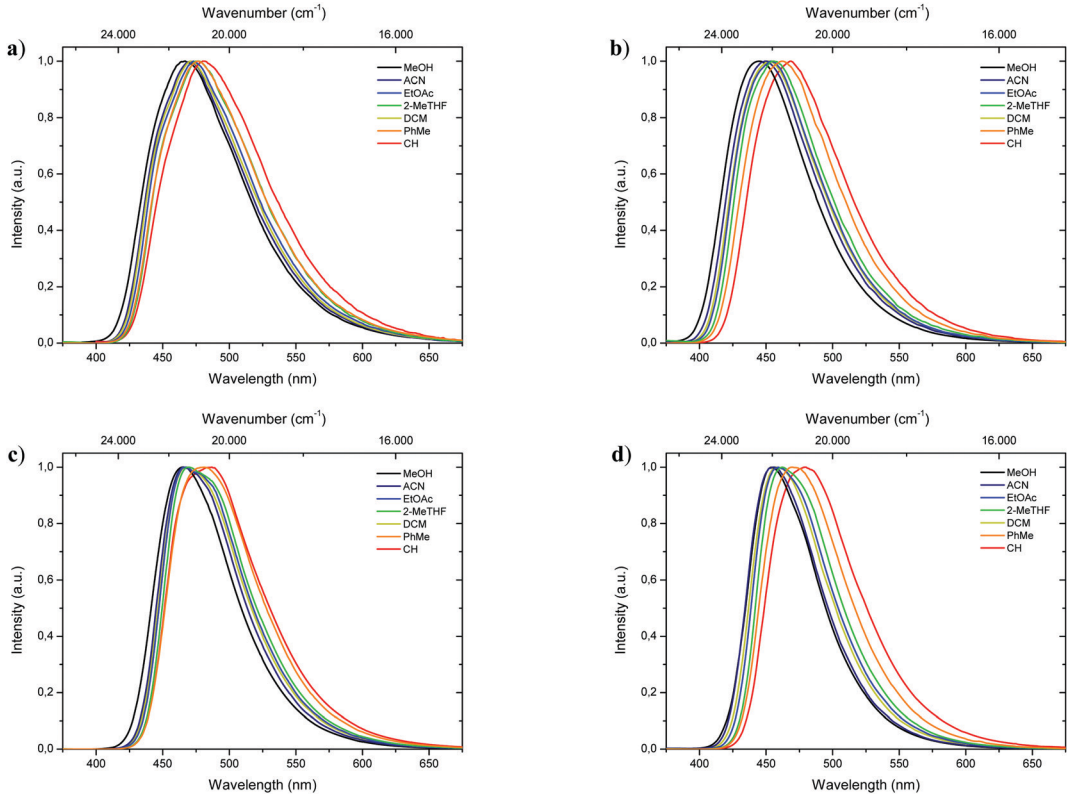

Fig. 4 Normalized emission spectra of **1-CN** (a), **2-CN** (b), **3-CN** (c) and **4-CN** (d) in various solvents.

analyzed fractions visible nano-aggregates have been formed, while massive nanoparticle formation has only taken place at f_w = 99% (Fig. 7; bottom). The nano-aggregated particles in f_w = 99% were analyzed in respect of their size using dynamic light scattering (DLS), revealing an average hydrodynamic radius of 706 ± 87.4 nm (Fig. 7b). Additionally, the emission properties of doped PMMA films with different weight concentration of **1-CN** (1 wt%, 10 wt% and 50 wt%) were examined

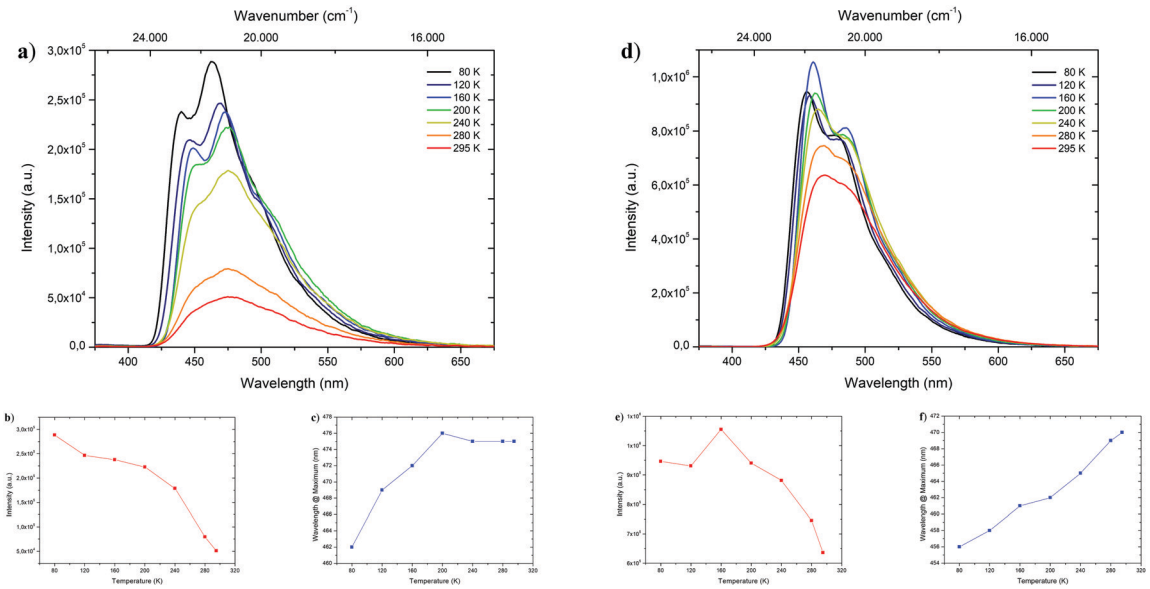

Fig. 5 Top: Temperature dependent emission spectra of **1-CN** (a) and **3-CN** (d) in deaerated 2-methyl tetrahydrofuran during heating from 80 K to 295 K with excitation at 321 and 327 nm, respectively. Bottom: Temperature dependent trends of intensity (**1-CN** (b) and **3-CN** (e)) and wavelength (**1-CN** (c) and **3-CN** (f)).

Table 2 Photophysical data of **1-CN**, **2-CN**, **3-CN** and **4-CN** measured in deaerated 2-MeTHF at 80 K

Compd	λ_{em} [nm]	τ [ns] (Rel%)
1-CN	440, 462	2.22 (36.4), 8.17 (51.7), 44.0 (11.9)
2-CN	444, (432)	1.22 (24.2), 5.58 (61.6), 23.0 (14.2)
3-CN	456, 476	1.95 (20.2), 7.29 (63.8), 24.1 (16.0)
4-CN	444, (462)	5.43 (100)

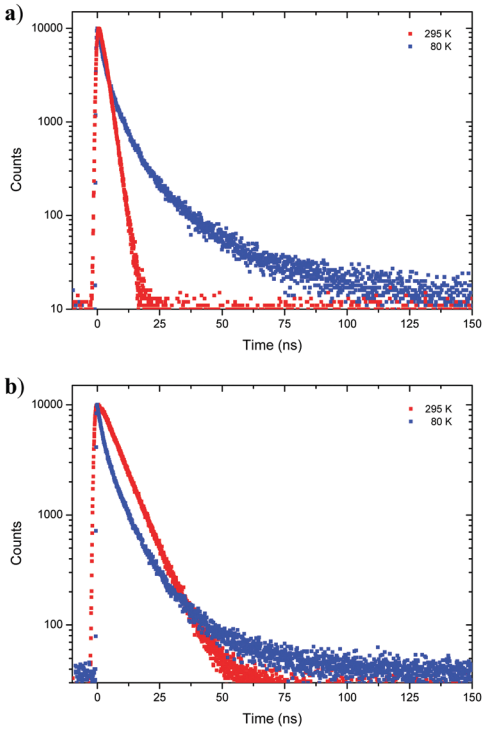

Fig. 6 Time resolved emission decay curves of **1-CN** (a) and **3-CN** (b) in deaerated 2-MeTHF at 80 K and 295 K.

(see the ESI,† Chapter 3.1.3). While films with 1 wt% and 10 wt% of **1-CN** exhibit similar blue emission, PMMA film with 50 wt% of **1-CN** showed bright green emission.

Solid-state emission

All phenols (**1-CN**, **2-CN**, **3-CN** and **4-CN**) exhibit bright luminescence in the solid-state to the naked eye by simple irradiation with a 366 nm UV-handlamp (Fig. 8; bottom). Therefore, investigations of the photophysical properties were conducted in the crystalline state for **1-CN**, **2-CN**, **3-CN** and in the microcrystalline state for **4-CN** (Fig. 8a). Optical properties of all phenols in the solid-state are listed in Table 3.

The brightest luminophore was **1-CN**, which showed a strong green-cyan emission with λ_{em} = 491 nm and Φ_F = 87.3% in the crystalline state. The fluorescence half lifetime was determined to τ = 13.3 ns. Dynamics studies (k_r = 0.66 × 10^8 s^{-1} and k_{nr} = 0.10 × 10^8 s^{-1}) revealed that the negligible nonradiative decay pathways yielded the high Φ_F. Noteworthily, semicrystalline powder of **1-CN** showed the same emission properties, indicating that no crystallization-induced emission enhancement (CIEE) has taken place (see the ESI,† Fig. S21). To the best of our knowledge **1-CN** represents the lowest molecular weight ESIPT-based fluorophore with a quantum yield above 85% in the solid-state. Also, **2-CN** displays strong blue emission with λ_{em} = 463 nm and Φ_F = 68.0% in the crystalline state and a high Stokes shift of 9.080 cm^{-1}. Based on these powerful solid-state emission properties and the weak emission in solution, both, **1-CN** and **2-CN** show a typical AIEE. Powerful green-cyan emission is observed for **3-CN** with λ_{em} = 494 nm and Φ_F = 74.1% in the crystalline state. A high fluorescence half lifetime of τ = 10.8 ns and low radiationless decay pathways (k_r = 0.69 × 10^8 s^{-1} and k_{nr} = 0.24 × 10^8 s^{-1}) verified the highly potent solid-state emission nature of **3-CN**. Together with its strong emission properties in solution, **3-CN** represents a dual state emission (DSE) luminophore. In comparison, **4-CN** showed relatively weak blue-cyan fluorescence in the microcrystalline state with λ_{em} = 473 nm and Φ_F = 14.7%. In consideration of the remarkable emission properties in solution, **4-CN** demonstrates aggregation-caused quenching (ACQ) character. As in solution, the large Stokes shifted emission is caused by an efficient proton transfer in the excited state, resulting in exclusive emission from the keto tautomer. CIE 1931 chromaticity coordinates (Fig. 8b) were calculated from the corresponding photoluminescence spectra, giving the following (x; y) values for **1-CN** (0.186; 0.387), **2-CN** (0.153; 0.168), **3-CN** (0.186; 0.417) and **4-CN** (0.142; 0.254). In the course of photophysical investigations, none of these analyzed emitters showed the tendency for photobleaching, neither in solution nor in the solid-state.

Single crystal packing

To better understand the emission characteristics of these highly efficient luminophores, suitable single crystals for X-ray diffraction were obtained for **1-CN**, **2-CN** and **3-CN** by evaporation of a concentrated dichloromethane solution. Unfortunately, **4-CN** showed only microcrystallite formation, which were not suitable for single crystal analysis. Crystallographic data are summarized in Table 4 and Tables S2–S19 (ESI†) and depicted in Fig. 9 and Fig. S108–S147 (ESI†).

The O1–H1···N2 hydrogen bond distances in **1-CN**, **2-CN** and **3-CN** were determined to be 1.670, 1.859 and 1.829 Å, respectively, while the corresponding angles are assigned to be 153.29°, 147.79°, and 148.01°. Dihedral angles between the phenol and oxazoline rings (*i.e.*, the C1–C2–C8–N2 angle) were found to be 0° for **1-CN**, −5.6° and −3.8° (C21–C22–C28–N22) for **2-CN** and −0.05° for **3-CN**, respectively. These crystal data revealed that the O–H···N hydrogen bond in **1-CN** is the strongest, which in turn facilitates intramolecular proton transfer to the adjacent nitrogen atom and rationalizes the extremely high Φ_F. To gain a deeper understanding of the increased Φ_F values in the solid-state, the crystal stacking modes were examined. **1-CN** (orthorhombic, *Pnma*), **2-CN** (triclinic, $P\bar{1}$) and **3-CN** (monoclinic, $P2_1/c$) exhibit different packing modes in their respective crystal lattice, including various types of intermolecular interactions. This variety of contacts leads to a restriction of intramolecular rotation and explains the increased Φ_F values in the solid-state. For **1-CN**, several intermolecular interactions,[33] like C–H···O (2.679 Å)

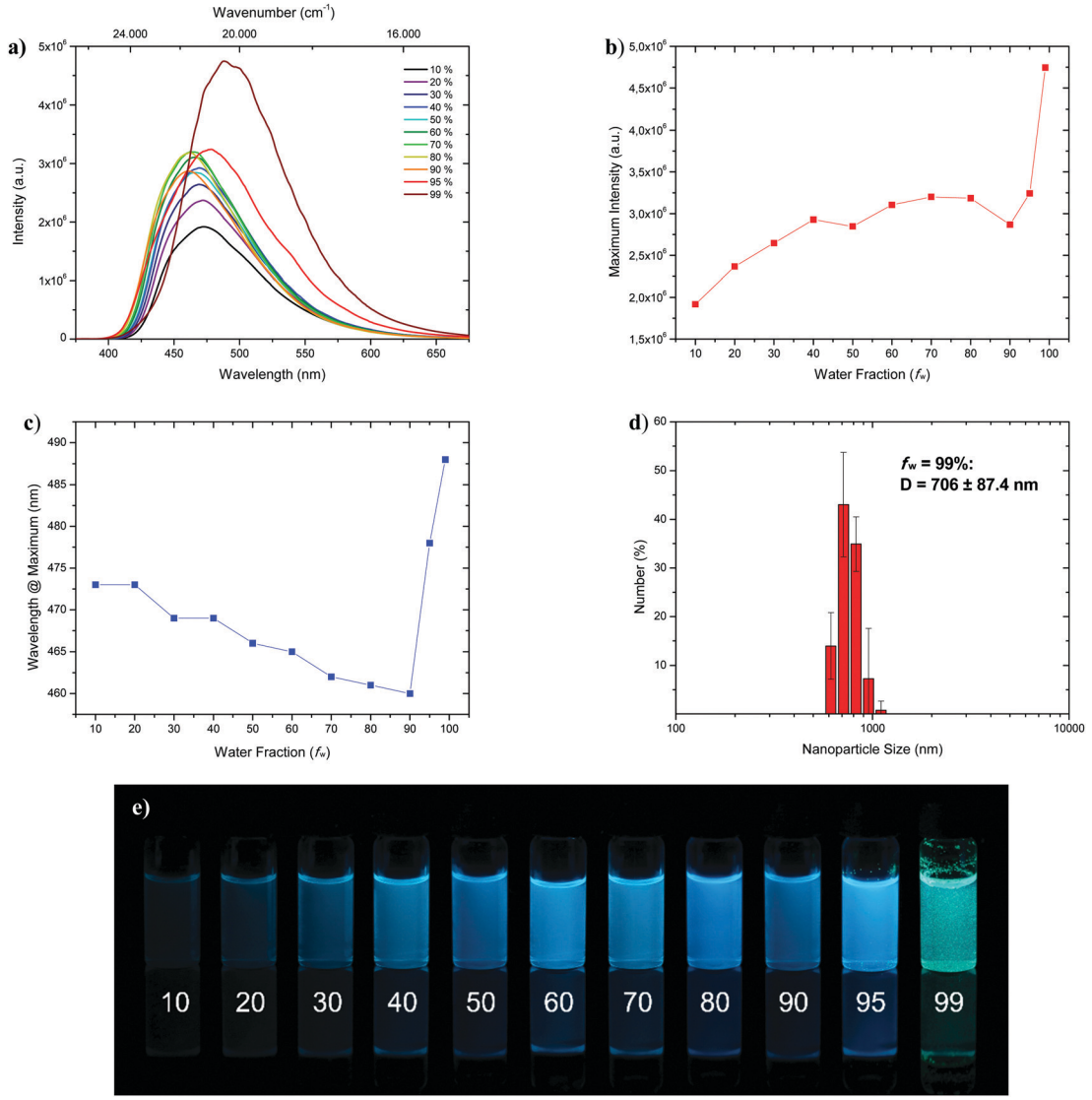

Fig. 7 (a) Emission spectra of **1-CN** in THF/water mixtures with differing water fraction (f_w in %) at a concentration of 4×10^{-5} mol L^{-1} under excitation with 321 nm. (b) Plot of maximum intensity *versus* water fraction (f_w). (c) Plot of wavelength at maximum *versus* water fraction (f_w). (d) DLS analysis of nanoparticle size distribution of fraction f_w = 99%. (e) Representative AIEE image of **1-CN** in THF/water mixtures with given water content (in %) under 366 nm irradiation.

or C–H···N (2.658 Å) are identified (see the ESI,† Fig. S120), while antiparallel molecule cross-stacking takes place along the *b*-axis in a sheet structure. Interplanar spacing is determined to 3.329 Å, whereas the adjacent π-skeleton distance is 3.586 Å with a slip angle of 68.2° (Fig. 9). Thus, relatively strong π–π-interactions lead to intense H-aggregation. Similarly, numerous intermolecular interactions, like C–H···O (2.584 Å) or C–H···N (2.627 Å) were detected for **2-CN** (see the ESI,† Fig. S131). Molecules are cross-stacked in an antiparallel sheet structure along the *a*-axis with interplanar spacing of 3.379 and 3.400 Å to the adjacent molecules, respectively. π-Skeleton distances of 3.476 Å and 3.565 Å with slip angles of 76.4° and 72.5° were determined, indicating strong H-aggregation.

In **3-CN** crystals, molecules are cross-stacked along the *b*-axis with an interplanar distance of 3.298 and 3.311 Å. Slip angles of 54.5° and 62.0° result in π-skeleton distances of 4.051 Å and 3.750 Å. In contrast to the previously discussed solid-state structures, sheet structure distortion of 12.4° is detected (see the ESI,† Fig. S145). Again, intermolecular interactions such as C–H···O (2.413 Å) or C–H···N (2.729 Å) lead to a restriction of intramolecular rotation, pointing to weak H-aggregation (see the ESI,† Fig. S146).

Interestingly, **1-CN** exhibits a bent nitrile bond (N1–C7–C_{ipso}) with an angle of 173.01°, whereas the respective bond in **2-CN** and **3-CN** is almost linear (see the ESI,† Tables S11 and S17). This observation can be explained through adjacent orbital interactions of the nonbonding orbital of the oxazoline-oxygen (O2) and a π*-orbital of the nitrile bond. The interaction energy was calculated by means of natural bond orbital (NBO) analysis and determined to 1.19 kcal mol^{-1} (see the ESI,† Chapter 6).

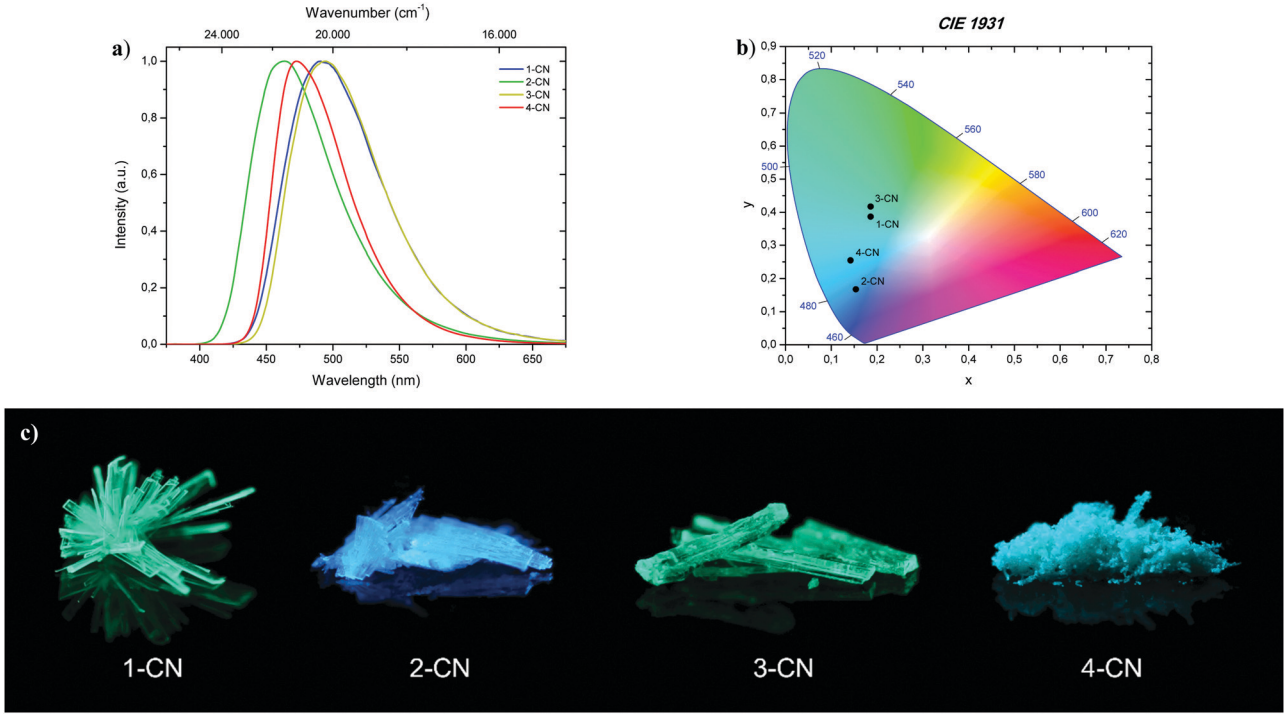

Fig. 8 (a) Normalized emission spectra of **1-CN**, **2-CN**, **3-CN** and **4-CN** in the solid-state. (b) CIE 1931 chromaticity plot with emission color coordinates of **1-CN**, **2-CN**, **3-CN** and **4-CN**. (c) Representative images of **1-CN**, **2-CN**, **3-CN** and **4-CN** in the solid-state under 366 nm irradiation.

Table 3 Photophysical data of **1-CN**, **2-CN**, **3-CN** and **4-CN** measured in the solid-state at 295 K

Compd	λ_{exc} [nm]	λ_{em} [nm]	$\Delta\tilde{\nu}$ [cm^{-1}]	Φ_F[a] [%]	τ [ns]	k_r[b] [10^8 s^{-1}]	k_{nr}[b] [10^8 s^{-1}]	x; y (CIE 1931)
1-CN	347	491	8.450	87.3	13.3	0.66	0.10	0.186; 0.387
2-CN	326	463	9.080	68.0	7.35	0.92	0.44	0.153; 0.168
3-CN	348	494	8.490	74.1	10.8	0.69	0.24	0.186; 0.417
4-CN	346	473	7.760	14.7	7.76	0.19	1.10	0.142; 0.254

[a] Absolute quantum yields were determined by using an integration sphere. [b] k_r (10^8 s^{-1}) and k_{nr} (10^8 s^{-1}) were calculated using the equations $k_r = \Phi_F/\tau$ and $k_{nr} = (1 - \Phi_F)/\tau$.

Table 4 Hydrogen bond (···) and crystal parameters of **1-CN**, **2-CN** and **3-CN**

	O1–H1···N2				
Compd	Length [Å]	Angle [°]	Dihedral angle C1–C2–C8–N2 [°]	Slip angles [°]	Plane distance [Å] with corresponding centroid–centroid distance ([Å])
1-CN	1.6704(3)	153.294(3)	0	68.2	3.329 (3.586)
2-CN	1.8592(19)	147.790(12)	−5.6(3); −3.8(3)	72.5; 76.4	3.379 (3.476); 3.400 (3.565)
3-CN	1.8289(11)	148.005(8)	−0.05(17)	54.5; 62.0	3.298 (4.051); 3.311 (3.750)

Commonly, H-aggregation results in diminished quantum yields, whereas J-aggregation results in improved emission.[34] **1-CN**, **2-CN** and **3-CN** exhibit high to extremely high quantum yields (Φ_F) in the solid-state, as already reported for other H-aggregated structures.[35] However, those literature known luminophores exhibit larger π-conjugated systems and are not constructed on a minimalistic single-benzene scaffold like the presented emitters. Usually, highly potent solid-state emitters based on a single-benzene core are commonly showing J-aggregation.[21–24] **1-CN** demonstrates its powerful emission (Φ_F = 87.3%) with a well-arranged crystal lattice, including a crystal system of relatively high symmetry (orthorhombic), several short intermolecular contacts (C–H···O/N) and strong π–π-interactions (centroid–centroid-distance = 3.586 Å). A short hydrogen bond distance (1.670 Å), a high hydrogen bond angle (153.29°) as well as a zero dihedral angle confirms the great solid-state emission potential of **1-CN**. The origin of the high photoluminescence quantum yield of **1-CN** can be multifarious. Intermolecular interactions in the crystal lattice such as C–H···N interactions or antiparallel coupling of local dipoles as described by Park and Adachi for styrylbenzene derivatives can cause such unusual optical behavior.[35b,d]

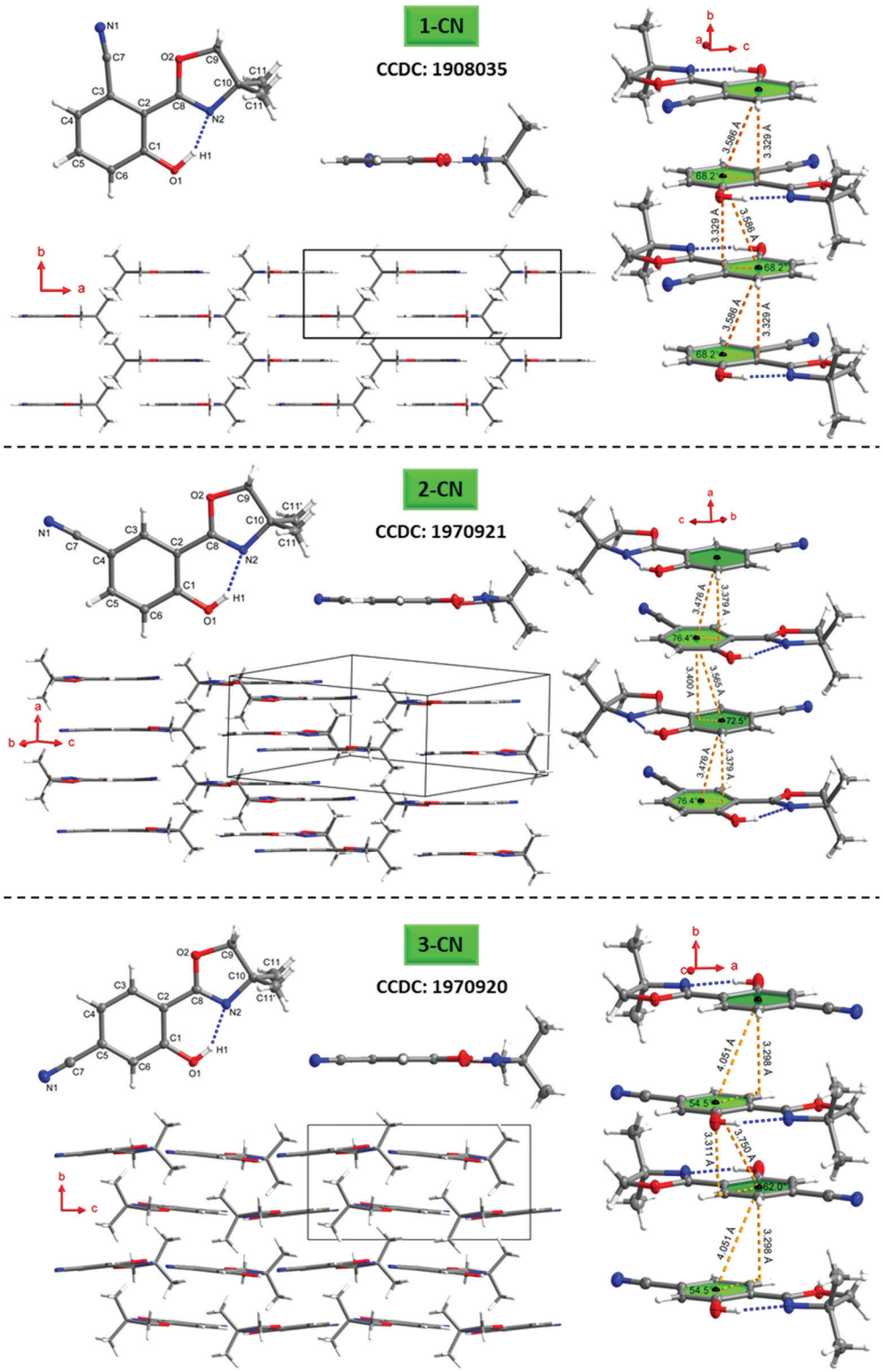

Fig. 9 Molecular structures of **1-CN** (top), **2-CN** (middle) and **3-CN** (bottom) showing 50% probability ellipsoids, including top view and sideview of the single structure, molecular packing as well as the π–π-interactions of adjacent molecules.

Finally, TGA/DSC measurements were conducted to investigate the thermal stability of the discussed luminophores. All of these novel low molecular weight phenols (M_W = 216.1), exhibit melting points T_M between 121 and 170 °C and decomposition temperatures T_{decomp} above 170 °C as determined by thermogravimetric analysis (TGA) and differential scanning calorimetry (DSC) (Table 5). The corresponding spectra are shown in the ESI† (Fig. S149–S152).

Table 5 Thermal stability properties

Compd	Onset/endset T [°C]	T_M [°C]	T_{decomp} [°C]
1-CN	199/233	172.4	229.5
2-CN	188/220	134.5	216.5
3-CN	190/224	122.2	219.9
4-CN	198/229	122.8	224.8

Calculated emission spectra

Fluorescence spectra of the keto tautomers of **1-CN**, **2-CN**, **3-CN** and **4-CN** were calculated with Time-Dependent Density Functional Theory (TDDFT)[36] at the TD-B97[37]/cc-pVDZ[38] level of theory to rationalize the experimental emission spectra. This level of theory was chosen because of the accurate reproduction of the experimental emission data (Fig. 10). Natural transition orbitals (NTOs)[39] were applied to characterize the first electronically excited singlet (S_1) state at the S_1 equilibrium geometry of the keto tautomer, out of which fluorescence takes place. NTOs typically allow the characterization of an electronically excited state *via* a single excitation from the Highest Occupied Natural Transition Orbital (HONTO) into the Lowest Unoccupied Natural Transition Orbital (LUNTO) with a remarkably high eigenvalue. In all cases considered here, the S_1 state can be characterized as an n–π*-state with eigenvalues > 0.99 (Fig. 11). The excitations are quite local, signifying only insignificant charge-transfer character. Due to the accurate reproduction of the experimental emission spectra by TDDFT, the calculated spectra provide further evidence that emission takes place from the S_1 state of the keto tautomer of each molecule presented here.

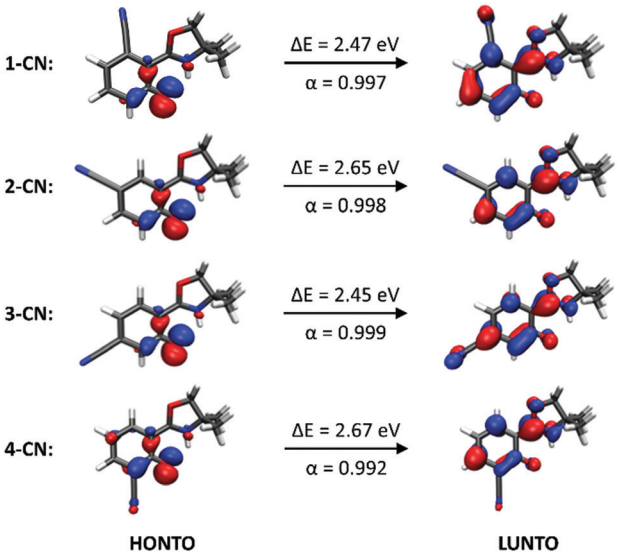

Fig. 11 Excitations from the Highest Occupied Natural Transition Orbital (HONTO) into the Lowest Unoccupied Natural Transition Orbital (LUNTO) that characterize the first electronically excited singlet (S_1) state at the S_1 equilibrium geometry of the keto tautomer, out of which the fluorescence of each of the four isomers takes place. ΔE is the electronic excitation energy of the S_1 state in the keto form and α is the eigenvalue of the HONTO → LUNTO transition.

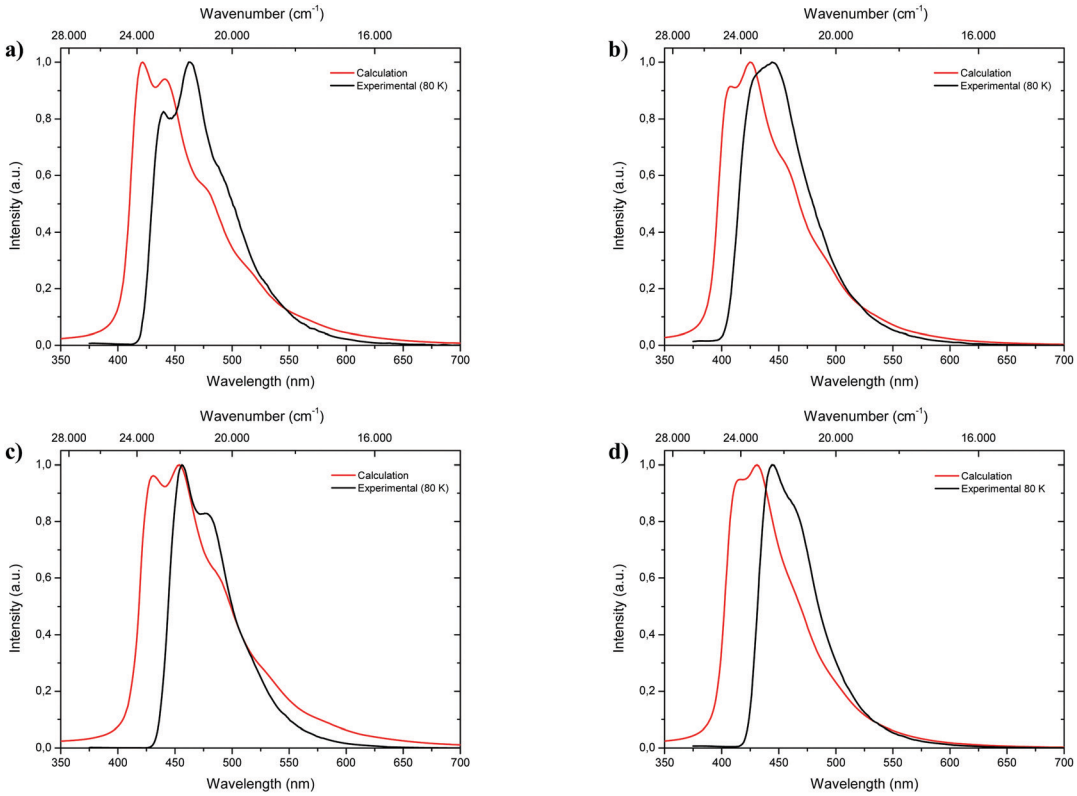

Fig. 10 Comparison of calculated fluorescence spectra (TD-B97/cc-pVDZ level of theory; red lines) with experimental emission spectra (black lines) measured in 2-MeTHF at 80 K of **1-CN** (a), **2-CN** (b), **3-CN** (c) and **4-CN** (d).

Conclusions

In summary, minimalistic, nitrile-substituted single-benzene ESIPT-based luminophores exhibiting powerful emission in the solid-state have been successfully synthesized and investigated towards their emission properties. Depending on the nitrile position, AIEE (**1-CN** and **2-CN**), DSE (**3-CN**) or ACQ characteristics (**4-CN**) with blue to green-cyan emission colors and high Stokes shifts were identified for all investigated fluorophores. Quantum yields are remarkably high and with **1-CN** the lowest molecular weight ESIPT-based luminophore with a quantum yield above 85% in the solid-state was discovered (M_W = 216.1; Φ_F = 87.3%). Through careful single crystal analysis, we identified the well-shaped molecular structure and the eminent organized crystal lattice as the origin of these outstanding photoluminescence properties. TDDFT calculated emission spectra gave evidence for emission from the S_1 state of the keto tautomer. This exceptionally straightforward concept for the creation of minimalistic, highly emissive fluorophores opens up the opportunity for future design studies yielding luminophores with superior properties. Applications of the discussed fluorophores in optoelectronic materials are underway in our laboratories.

Conflicts of interest

There are no conflicts to declare.

Acknowledgements

We thank Prof. Dr Nadja-C. Bigall, Dr Dirk Dorfs, and Pascal Rusch (all from Leibniz University Hannover) for supporting the photophysical measurements.

References

1 (*a*) R. Long, C. Tang, J. Xu, T. Li, C. Tong, Y. Guo, S. Shi and D. Wang, *Chem. Commun.*, 2019, **55**, 10912; (*b*) R. T. K. Kwok, C. W. T. Leung, J. W. Y. Lam and B. Z. Tang, *Chem. Soc. Rev.*, 2015, **44**, 4228; (*c*) H. Kobayashi, M. Ogawa, R. Alford, P. L. Choyke and Y. Urano, *Chem. Rev.*, 2010, **110**, 2620; (*d*) L. D. Lavis and R. T. Raines, *ACS Chem. Biol.*, 2008, **3**, 142.

2 (*a*) X. Li, X. Gao, W. Shi and H. Ma, *Chem. Rev.*, 2014, **114**, 590; (*b*) S. W. Thomas, G. D. Joly and T. M. Swager, *Chem. Rev.*, 2007, **107**, 1339; (*c*) L. Basabe-Desmonts, D. N. Reinhoudt and M. Crego-Calama, *Chem. Soc. Rev.*, 2007, **36**, 993; (*d*) R. Martínez-Máñez and F. Sancenón, *Chem. Rev.*, 2003, **103**, 4419; (*e*) A. P. de Silva, H. Q. N. Gunaratne, T. Gunnlaugsson, A. J. M. Huxley, C. P. McCoy, J. T. Rademacher and T. E. Rice, *Chem. Rev.*, 1997, **97**, 1515.

3 (*a*) H. Yersin, *Highly Efficient OLEDs with Phosphorescent Materials*, Wiley-VCH, Hoboken, 2008; (*b*) K. Müllen and U. Scherf, *Organic Light-Emitting Devices. Synthesis, Properties, and Applications*, Wiley-VCH, Weinheim, 2006; (*c*) R. H. Friend, R. W. Gymer, A. B. Holmes, J. H. Burroughes, R. N. Marks, C. Taliani, D. D. C. Bradley, D. A. D. Santos, J. L. Brédas, M. Lögdlund and W. R. Salaneck, *Nature*, 1999, **397**, 121.

4 (*a*) M. D. Watson, A. Fechtenkötter and K. Müllen, *Chem. Rev.*, 2001, **101**, 1267; (*b*) R. E. Martin and F. Diederich, *Angew. Chem., Int. Ed.*, 1999, **38**, 1350.

5 (*a*) O. Ostroverkhova, *Chem. Rev.*, 2016, **116**, 13279; (*b*) H. Meier, *Angew. Chem., Int. Ed.*, 2005, **44**, 2482; (*c*) R. Gompper and H.-U. Wagner, *Angew. Chem., Int. Ed. Engl.*, 1988, **27**, 1437.

6 J. Mei, N. L. C. Leung, R. T. K. Kwok, J. W. Y. Lam and B. Z. Tang, *Chem. Rev.*, 2015, **115**, 11718.

7 J. Mei, Y. Hong, J. W. Y. Lam, A. Qin, Y. Tang and B. Z. Tang, *Adv. Mater.*, 2014, **26**, 5429.

8 B. Z. Tang and A. Qin, *Aggregation-Induced Emission. Fundamentals*, Wiley, John Wiley & Sons Inc., Chichester, 2013.

9 (*a*) B.-K. An, J. Gierschner and S. Y. Park, *Acc. Chem. Res.*, 2012, **45**, 544; (*b*) D. Oelkrug, A. Tompert, J. Gierschner, H.-J. Egelhaaf, M. Hanack, M. Hohloch and E. Steinhuber, *J. Phys. Chem. B*, 1998, **102**, 1902.

10 Z. Zhao, J. W. Y. Lam and B. Z. Tang, *J. Mater. Chem.*, 2012, **22**, 23726.

11 S. Benson, A. Fernandez, N. D. Barth, F. de Moliner, M. H. Horrocks, C. S. Herrington, J. L. Abad, A. Delgado, L. Kelly, Z. Chang, Y. Feng, M. Nishiura, Y. Hori, K. Kikuchi and M. Vendrell, *Angew. Chem., Int. Ed.*, 2019, **58**, 6911.

12 M. Shimizu and T. Hiyama, *Chem. – Asian J.*, 2010, **5**, 1516.

13 (*a*) A. C. Sedgwick, L. Wu, H.-H. Han, S. D. Bull, X.-P. He, T. D. James, J. L. Sessler, B. Z. Tang, H. Tian and J. Yoon, *Chem. Soc. Rev.*, 2018, **47**, 8842; (*b*) V. S. Padalkar and S. Seki, *Chem. Soc. Rev.*, 2016, **45**, 169; (*c*) A. P. Demchenko, K.-C. Tang and P.-T. Chou, *Chem. Soc. Rev.*, 2013, **42**, 1379; (*d*) J. E. Kwon and S. Y. Park, *Adv. Mater.*, 2011, **23**, 3615.

14 P. F. Barbara, P. K. Walsh and L. E. Brus, *J. Phys. Chem.*, 1989, **93**, 29.

15 H.-Q. Yin, F. Yin and X.-B. Yin, *Chem. Sci.*, 2019, **10**, 11103.

16 (*a*) K. Benelhadj, W. Muzuzu, J. Massue, P. Retailleau, A. Charaf-Eddin, A. D. Laurent, D. Jacquemin, G. Ulrich and R. Ziessel, *Chem. – Eur. J.*, 2014, **20**, 12843; (*b*) H. Shono, T. Ohkawa, H. Tomoda, T. Mutai and K. Araki, *ACS Appl. Mater. Interfaces*, 2011, **3**, 654; (*c*) K.-C. Tang, M.-J. Chang, T.-Y. Lin, H.-A. Pan, T.-C. Fang, K.-Y. Chen, W.-Y. Hung, Y.-H. Hsu and P.-T. Chou, *J. Am. Chem. Soc.*, 2011, **133**, 17738; (*d*) S. Park, J. E. Kwon, S. H. Kim, J. Seo, K. Chung, S.-Y. Park, D.-J. Jang, B. Milián Medina, J. Gierschner and S. Y. Park, *J. Am. Chem. Soc.*, 2009, **131**, 14043.

17 Y. Zhang, H. Yang, H. Ma, G. Bian, Q. Zang, J. Sun, C. Zhang, Z. An and W.-Y. Wong, *Angew. Chem., Int. Ed.*, 2019, **58**, 8773.

18 (*a*) T. Mutai, H. Shono, Y. Shigemitsu and K. Araki, *CrystEngComm*, 2014, **16**, 3890; (*b*) T. Mutai, H. Tomoda, T. Ohkawa, Y. Yabe and K. Araki, *Angew. Chem., Int. Ed.*, 2008, **47**, 9522.

19 (*a*) T. Mutai, T. Ohkawa, H. Shono and K. Araki, *J. Mater. Chem. C*, 2016, **4**, 3599; (*b*) T. Mutai, H. Sawatani, T. Shida, H. Shono and K. Araki, *J. Org. Chem.*, 2013, **78**, 2482.

20 S. Park, J. E. Kwon, S.-Y. Park, O.-H. Kwon, J. K. Kim, S.-J. Yoon, J. W. Chung, D. R. Whang, S. K. Park, D. K. Lee, D.-J. Jang, J. Gierschner and S. Y. Park, *Adv. Opt. Mater.*, 2017, **5**, 1700353.

21 B. Tang, H. Liu, F. Li, Y. Wang and H. Zhang, *Chem. Commun.*, 2016, **52**, 6577.

22 M. Shimizu, Y. Takeda, M. Higashi and T. Hiyama, *Angew. Chem., Int. Ed.*, 2009, **121**, 3707.
23 T. Beppu, K. Tomiguchi, A. Masuhara, Y.-J. Pu and H. Katagiri, *Angew. Chem., Int. Ed.*, 2015, **54**, 7332.
24 B. Tang, C. Wang, Y. Wang and H. Zhang, *Angew. Chem., Int. Ed.*, 2017, **56**, 12543.
25 Z. Xiang, Z.-Y. Wang, T.-B. Ren, W. Xu, Y.-P. Liu, X.-X. Zhang, P. Wu, L. Yuan and X.-B. Zhang, *Chem. Commun.*, 2019, **55**, 11462.
26 D. Yao, S. Zhao, J. Guo, Z. Zhang, H. Zhang, Y. Liu and Y. Wang, *J. Mater. Chem.*, 2011, **21**, 3568.
27 W.-T. Chuang, C.-C. Hsieh, C.-H. Lai, C.-H. Lai, C.-W. Shih, K.-Y. Chen, W.-Y. Hung, Y.-H. Hsu and P.-T. Chou, *J. Org. Chem.*, 2011, **76**, 8189.
28 D. Göbel, N. Clamor, E. Lork and B. J. Nachtsheim, *Org. Lett.*, 2019, **21**, 5373.
29 D. Göbel, N. Clamor and B. J. Nachtsheim, *Org. Biomol. Chem.*, 2018, **16**, 4071.
30 K. Schwekendiek and F. Glorius, *Synthesis*, 2006, 2996.
31 R. Misra and S. P. Bhattacharyya, *Intramolecular Charge Transfer*, Wiley-VCH, Weinheim, 2018.
32 (*a*) Q. Yu, X. Zhang, S.-T. Wu, H. Chen, Q.-L. Zhang, H. Xu, Y.-L. Huang, B.-X. Zhu and X.-L. Ni, *Chem. Commun.*, 2020, **56**, 2304; (*b*) T. Zhang, L. Wen, G. Liu, J. Yan, X. Liu, K. Zheng and N. Zhang, *Chem. Commun.*, 2019, **55**, 13713.
33 H. Lin, X. Chang, D. Yan, W.-H. Fang and G. Cui, *Chem. Sci.*, 2017, **8**, 2086.
34 (*a*) N. J. Hestand and F. C. Spano, *Chem. Rev.*, 2018, **118**, 7069; (*b*) D. Möbius, *Adv. Mater.*, 1995, **7**, 437.
35 (*a*) Y. Niu, R. Wang, P. Shao, Y. Wang and Y. Zhang, *Chem. – Eur. J.*, 2018, **24**, 16670; (*b*) S.-J. Yoon and S. Park, *J. Mater. Chem.*, 2011, **21**, 8338; (*c*) S.-J. Yoon, J. W. Chung, J. Gierschner, K. S. Kim, M.-G. Choi, D. Kim and S. Y. Park, *J. Am. Chem. Soc.*, 2010, **132**, 13675; (*d*) R. Kabe, H. Nakanotani, T. Sakanoue, M. Yahiro and C. Adachi, *Adv. Mater.*, 2009, **21**, 4034; (*e*) U. Rösch, S. Yao, R. Wortmann and F. Würthner, *Angew. Chem., Int. Ed.*, 2006, **45**, 7026.
36 R. Bauernschmitt and R. Ahlrichs, *Chem. Phys. Lett.*, 1996, **256**, 454.
37 A. D. Becke, *J. Chem. Phys.*, 1997, **107**, 8554.
38 T. H. Dunning, *J. Chem. Phys.*, 1989, **90**, 1007.
39 R. L. Martin, *J. Chem. Phys.*, 2003, **118**, 4775.